Applied Surface Science 567 (2021) 150791

Contents lists available at ScienceDirect

Applied Surface Science

journal homepage: www.elsevier.com/locate/apsusc

Full Length Article

Electrochemical and morphological layer-by-layer characterization of electrode interfaces during a label-free impedimetric immunosensor build-up: The case of ochratoxin A

Rocco Cancelliere [a,b], David Albano [a], Benedetta Brugnoli [a,c], Katia Buonasera [a], Gabriella Leo [d], Andrea Margonelli [a], Giuseppina Rea [a,*]

[a] Institute of Crystallography, CNR, Via Salaria Km 29,300, 00015 Monterotondo, Rome, Italy
[b] Department of Chemical Science and Technologies, University of Rome "Tor Vergata", Via Della Ricerca Scientifica 1, 00133 Rome, Italy
[c] Department of Chemistry, Sapienza University of Rome, Piazzale Aldo Moro 5, Rome 00185, Italy
[d] Institute for the Study of Nanostructured Materials, CNR, Via Salaria Km 29,300, 00015 Monterotondo, Rome, Italy

ARTICLE INFO

Keywords:
Electron transfer kinetics
Diffusivity process
Label-free immunosensors
Ochratoxin A immunosensor
Contact angle

ABSTRACT

In this paper, we provide an in-depth electrochemical characterization of a label-free impedimetric immunosensor for rapid detection of ochratoxin A. The sensor was based on a carbodiimide-mediated amide coupling reaction to immobilize a specific ochratoxin A antibody onto 4-mercaptobenzoic acid-modified commercial screen-printed gold electrode. Different variables affecting the performance of the developed sensor were optimized. Cyclic voltammetry and electrochemical impedance spectroscopy were used to analyse modifications of the interfacial properties occurring at each step of the biosensor assembly. The free electrode surface area, the diffusion coefficient, the peak-to-peak separation, the heterogeneous electron transfer constant, and charge transfer resistance have been calculated and compared. The decrease of charge transfer resistance values was linearly proportional to the ochratoxin A concentration in the range of 0.37– 2.86 ng/mL, with a detection limit of 0.19 ng/mL, a limit of quantification of 0.40 ng/mL, very good selectivity, reproducibility, and storage stability in the absence of antifouling agents. Surface morphology and topographic data at each step of the immunosensor assembly were studied by Atomic Force Microscopy, which also provided information on the specific binding of ochratoxin A. Finally, contact angle measurements revealed the hydrophilicity evolution of the surface during sensor assembly enabling OTA binding.

1. Introduction

The development of electrochemical surface investigation provided the basis for a mechanistic understanding of the electrochemical processes occurring at the solid/liquid interface providing information on charge transfer kinetics [1]. This knowledge laid foundations for the development of important technological applications including, among others, electrochemical sensors for environmental monitoring or diagnostics [2].

In the last two decades, the manufacture of electrochemical sensors has been revolutionized by the screen-printing technology [3], promoting the development of integrated measurement devices, e.g. lab-on-a-chip or point-of-care instruments for medical purposes [4-6]. The agri-food business also requires the adoption of reliable sensing systems for the fast detection of food and environmental contaminants possibly affecting human health [7]. In this context, the availability of miniaturized, fast-response, *on-site* detection systems represents complementary useful tools to the more complex and expensive chromatographic and spectroscopic techniques which are the golden standard of conventional analyses [8].

Screen-printed-electrodes (SPEs) are miniaturized, robust, and usually low-cost platforms offering versatile sensor design and transduction systems. The possibility to modify the electrode surface with a plethora of chemically different molecules enables the construction of selective platform for the detection of a wide variety of analytes, *de facto* expanding the application field of electrochemical sensors. Herein, the formation of self-assembled monolayers (SAMs), achieved by either adsorption or electrodeposition methods, is the basis for further

* Corresponding author.
E-mail address: giuseppina.rea@ic.cnr.it (G. Rea).

https://doi.org/10.1016/j.apsusc.2021.150791
Received 27 May 2021; Received in revised form 23 July 2021; Accepted 27 July 2021
Available online 31 July 2021

functionalization steps conferring novel chemical, biological or mechanical interfacial properties to the bare electrode for targeted analyses.

To probe the changes of the electrode/electrolyte interface properties occurring during sensor assembly and functioning, different non-destructive electrochemical techniques, including cyclic voltammetry (CV) and electrochemical impedance spectroscopy (EIS), are typically used [9-11]. Atomic Force Microscopy (AFM) is often used to explore the morphological and topological changes occurring during the deposition of monolayers [8,12,13]. Moreover, information on surface wetting by using contact-angle measurements [14] could also provide crucial information for construction of biosensors.

In the field of immunosensors, where an antibody is used to recognize a specific antigen (analyte), the EIS technique enables a label-free detection of the immunocomplex, simplifying the measurement and reducing costs due to the molecular labels [15,16].

The detection of toxins is of particular relevance for food safety and several toxins-sensitive sensors have been developed over the years, as reviewed in different works [16,17]. Ochratoxin A (OTA) is a mycotoxin produced by fungal species of the genera *Penicillium* and *Aspergillus* [18], contaminating several food commodities worldwide [19]. OTA has been reported as hepatotoxic, nephrotoxic, immune suppressant, teratogenic, and fetotoxic agent [20], and it has also been classified as a possible human carcinogen (Group 2B) by the International Agency for Research on Cancer [21]. Due to OTA potential toxicity, several countries have implemented specific regulations for maximum residue levels (MRL) in food products. European Union (EU) set the maximum OTA concentration in cereals to 5 ppb, 2 ppb in wine (or grape juice), and 5 ppb in coffee products [22]. In 1999 the Italian Ministry of Health adopted the limit of 3 ppb for cereal derivatives and established the Italian limit of 0.5 ppb for baby foods [23].

In the frame of a regional funded project aiming to construct a portable, electrochemical multi-transduction device for environmental and food safety monitoring, we set-up a model sensor to verify and test the novel constructed instrument. In this work, we report about the deep electrochemical characterization of screen-printed gold electrode (SPGE) interface during the multistep OTA-biosensor build-up. The biosensor was assembled on gold serigraphic platforms that are amid the most versatile and customizable enabling surface coatings with a plethora of thiol-conjugated bio/materials for the construction of a wide variety of electrochemical sensing platforms [24]. In particular, commercially available, low-priced SPGEs were exploited to fabricate an impedimetric label-free immunosensor for OTA detection, optimizing previously reported procedures [25-27]. Exploring the surface properties and morphology by CV, EIS, AFM, and contact angle measurements, a reliable and efficient protocol was set-up overcoming some drawbacks introduced by the printing technology (e.g., roughness, non-uniformity) which often hamper the biosensor functionality.

2. Experimental

2.1. Materials

All chemicals from commercial sources were of analytical grade. 4-Mercaptobenzoic acid (MBA, 99%), N-hydroxysuccinimide (NHS, 98%), N-(3-Dimethylaminopropyl)-N′-ethyl carbodiimide (EDC, ≥97%), Ethanolamine ($EtNH_2$, ≥99.5%), 2-(N-morpholino) ethane sulfonic acid (MES, ≥99%), Potassium hexacyanoferrate (III) ($[Fe(CN)_6]^{3-}$, ferrocyanide, ≥99%), Potassium hexacyanoferrate (II) ($[Fe(CN)_6]^{4-}$, ferricyanide, ≥99%), Isopropanol (IpOH), Ethanol (EtOH, ≥99.8%), Sulfuric acid (H_2SO_4, 95–99%), Sodium hydrogen phosphate (Na_2HPO_4, ≥99%), Potassium dihydrogen orthophosphate (KH_2PO_4, ≥99%), Potassium chloride (KCl, ≥99%), and OTA from *Aspergillus ochraceus* were purchased from Sigma-Aldrich (St. Louis, Mo, USA). Anti-Ochratoxin A antibody (Ab-OTA) (5 mg/mL) was purchased from Abcam (Cambridge, United Kingdom). Na_2HPO_4 and KH_2PO_4 were used to prepare 0.1 M Phosphate Buffer (PB) or 0.1 M Phosphate Buffer Saline by adding 0.1 M KCl (PBS), and the pH was adjusted according to the experiment requirements indicated in the text. A buffer solution 0.1 M MES pH 5.5 was used to prepare OTA dilutions. Aflatoxin B_1, B_2, G_2 (purchased from Sigma-Aldrich) were kindly provided by Prof. Laura Micheli. Milli-Q-purified water Millipore (18.2 MΩ cm) was used for the preparation of all buffer solutions.

2.2. Apparatus

The electrochemical measurements were performed by using the portable potentiostat PalmSens4 (Palm Instrument, The Netherlands) connected to a laptop and controlled by PSTrace software. Disposable SPGEs (DRP-250AT) were purchased from Methrom Italiana S.r.l.

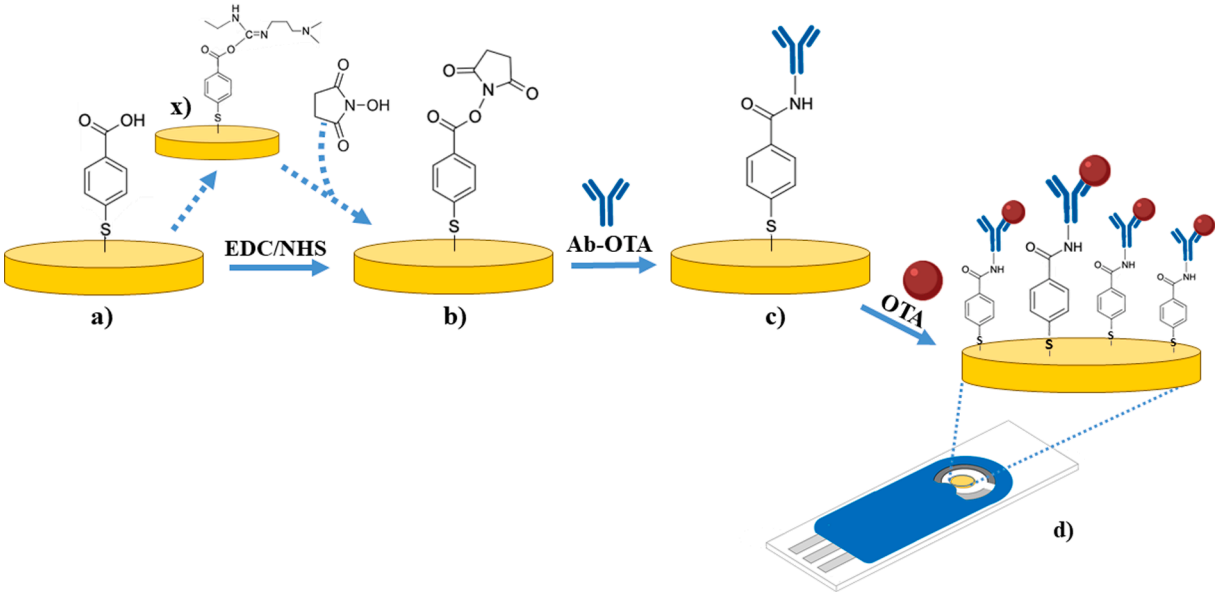

Fig. 1. Schematic representation of the SPGE-based immunosensor assembly for OTA detection. The EDC-mediated amide coupling reaction on electrode surface is depicted from a) MBA functionalization of the SPGE to b) EDC/NHS reaction, including the initial incorporation of EDC, to x) generating the active O-acylisourea intermediates. The Ab-OTA covalent immobilization and subsequent OTA binding are depicted in c) and d), respectively.

(Rome, Italy). The SPGEs are made up of ceramic (L33 × W10 × H0.5 mm) with silver electric contacts and incorporate a conventional three-electrode configuration consisting in a working (gold, 4 mm diameter), counter (platinum) and reference (pseudo-silver) electrode.

Atomic Force Microscopy (AFM) topographic images were recorded in air in tapping mode by DIMENSION AFM system (BRUKER, USA) equipped with a Si tips (BRUKER, TESP-V2) having nominal curvature radius of 7 nm and 37 N/m nominal elastic constant. Height, peak force error and in-phase images were also taken from selected samples in Peak Force Tapping® mode by a Multimode 8 microscope (BRUKER, USA) equipped with Silicon Nitride probes (SCANASYST AIR, BRUKER, USA) having 2 nm nominal curvature radius and 0.3 N/m elastic constant.

2.3. Preparation of OTA-Immunosensor

SPGEs based immunosensors for detection of OTA were prepared following a multi-step procedure. Initially, the SPGEs were cleaned in isopropanol for 10 min to remove any impurities related to human contact or dust, rinsed with Milli-Q water, and dried under N_2 flow. All the conditions adopted during the immunosensor fabrication steps and reported below have been optimised as reported in the Supplementary Materials. Subsequently, each electrode was treated by using 10 scans of CV in the range between −0.3 V and 1.4 V, with a scan rate of 100 mV/s, using 0.05 M H_2SO_4 as electrolyte (Fig. S1; Table S1). The electrodes were hence rinsed twice with 500 µL of acidified water, once with 500 µL Milli-Q water, and dried under N_2 flow. Then, a solution of 0.005 M MBA in EtOH was electrodeposited on SPGEs surface by using chronoamperometry (CA) under a constant potential of 1.2 V for 20 min (Table S2). The electrodes were hence rinsed twice with 500 µL of EtOH solution, once with 500 µL Milli-Q water, and dried under N_2 flow. Carboxylic groups of electrodeposited MBA were, hence, activated by dropping 10 µL of EDC/NHS water solution (1:1 v/v, freshly prepared by mixing 0.005 M EDC and 0.005 M NHS), on working electrode and let it to react for 20 min in the dark. Electrodes were, hence, rinsed three times with 500 µL of Milli-Q water and dried under N_2 flow. The immobilization of Ab-OTA was carried out by dropping 10 µL of Ab-OTA solution (5 µg/mL) in 0.1 M PBS pH 5.5 on functionalised SPGEs (Fig. S2-S4). The electrodes were kept under constant agitation at room temperature in the dark for 18 hr. Afterwards the electrodes were washed twice with 500 µL of PBS pH 7, once with 500 µL of PBS pH 7 plus 0.05% Tween 20 to reduce a-specific binding and let to dry at room temperature. Successively, 100 µL of 1 M $EtNH_2$ solution pH 8.5 were dropped onto the modified surface and incubated at room temperature in the dark for 15 min to block unreacted active sites. After washing two times with 500 µL of PBS pH 7 and once with PBS pH 5.5, 10 µL of different OTA concentrations in the range 0–10 ng/mL were dropped on the working electrode, incubated in the dark for 1 hr, washed three times with 500 µL of PBS pH 7, and analysed (Fig. 1; Fig. S5).

2.4. Experimental measurements

The OTA-immunosensor construction was electrochemically characterised step by step by CV and EIS. The measurements were carried out using a solution of 0.005 M ferro/ferricyanide (1:1 v/v) in 0.1 M PBS pH 7.0 as redox probe at room temperature. In the case of EIS measurements, a frequency range between 0.1 Hz and 10^5 Hz, 10 frequencies per decade, at an open circuit potential, with a voltage amplitude of 0.01 V, was used, while data fitting was provided by Z-View software (Scribner Associates Inc.). CV measurements were performed in the range −0.35 to 0.6 V vs reference electrode with a scan rate of 100 mV/s.

The OTA-immunosensor construction was monitored by AFM measurements performed soon after each deposition step to avoid possible sample degradation. For each step 512x512 point height images were recorded in tapping mode. Scans from 4 to 5 randomly chosen locations of the electrode and with different scan sizes were collected in order to check the lateral uniformity of the surface morphology. Dimensions of the scans varied between 3 × 3 µm and 10 × 10 µm.

AFM image were also recorded at better resolution (1024x1024 points) in Peak Force Tapping® mode after Ab-OTA immobilization on MBA, and OTA specific binding on Ab-OTA. Root mean square (RMS) roughness and peak-to-peak height of all the resulting scan images were calculated by Nanoscope Analysis software (BRUKER, USA). Profile of cluster were obtained by ImageSXM software [28].

To examine SPGEs wettability changes occurring after each deposition step, static contact angle was measured by the drop method. Measurements were performed on Milli-Q water droplet (V = 5 μL) deposited on and covering the entire working electrode (WE) surface, at room temperature. Images were captured and elaborated with the Motic Images Plus 2.0 (China) to define the base length (D) and height (h) of the drop. The contact angle (θ) was determined as follows:

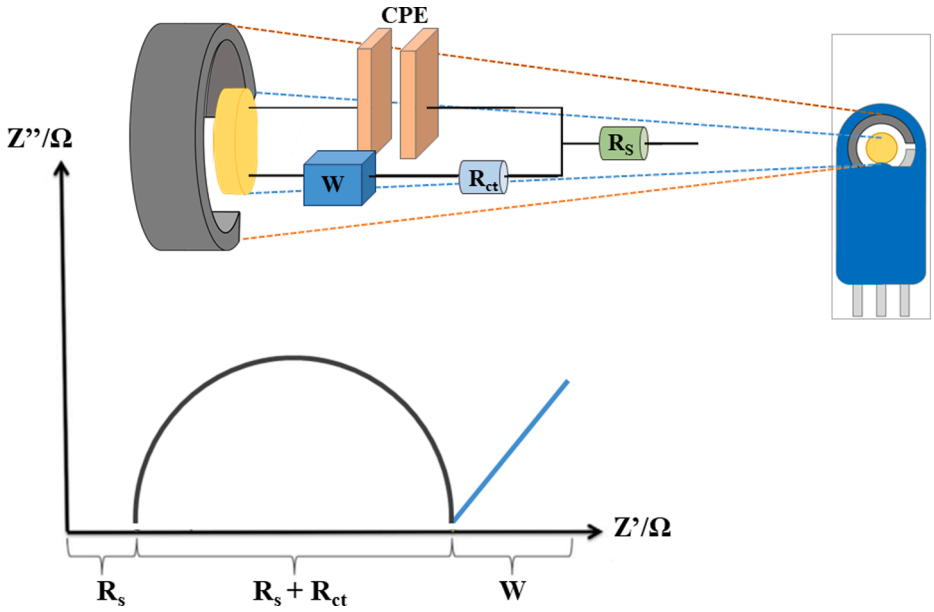

Fig. 2. Schematic representation of equivalent Randles circuit. R_s: Ohmic resistance; R_{ct}: charge transfer resistance; W: Warburg impedance; CPE: constant phase element.

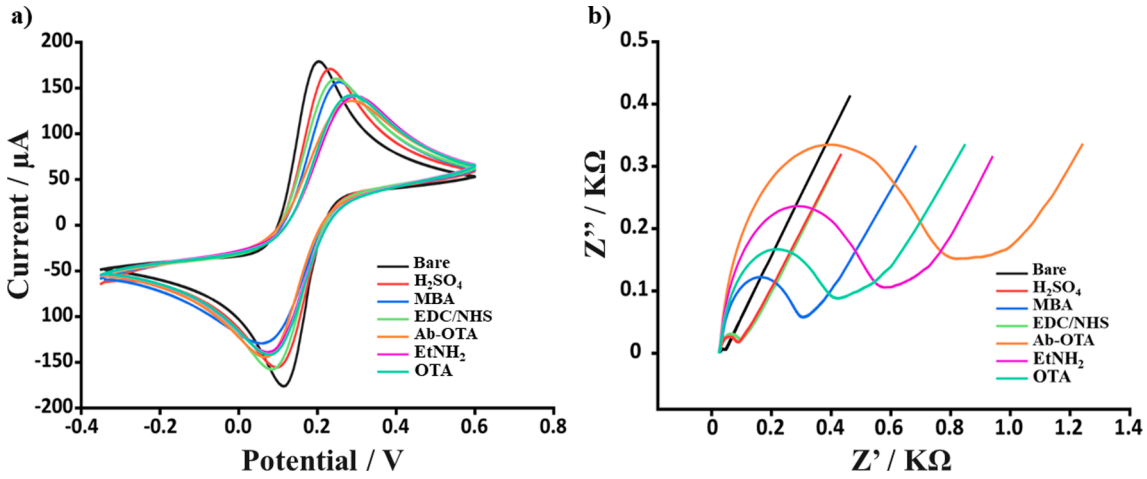

Fig. 3. Electrochemical characterization of electrode interfaces during the multistep biosensor build-up. a) Cyclic voltammograms and b) Nyquist's Plot recorded in 0.005 M $[Fe(CN)_6]^{4-/3-}$ in 0.05 M PBS (OTA 5 ng/ml). Curves of one representative SPGE fabricated sensor of at least 6 analysed SPGEs are presented.

$$\theta = 2\tan^{-1}\left(\frac{2h}{D}\right) \quad (1)$$

Each reported contact angle was the mean value of four measurements (Table S4).

2.5. Analytical parameters calculation

Once optimized all the main experimental parameters affecting the performance of the device, the analytical performance of the platform was investigated measuring the signal change obtained with different concentrations of OTA. The calibration curve was, hence, obtained by plotting the value of OTA concentrations in semilogarithmic scale versus ΔR_{ct}. ΔR_{ct} was calculated by the following equation:

$$\Delta R_{ct} = R_{ct_{Ab-OTA}} - R_{ct_{OTA}} \quad (2)$$

where $R_{ct_{Ab-OTA}}$ is the value of charge transfer resistance when Ab-OTA is immobilized on the electrode surface, and $R_{ct_{OTA}}$ is the value of charge transfer resistance after immune-complex formation. The standard curves were fitted using a Four Parameter Logistic (4PL) Regression according to Warwick 1996 [29].

The limit of detection (LOD) and the limit of quantification (LOQ) were defined as the decrease of the maximum signal equal to three and ten times, respectively, the value of the standard deviations measured in the absence of OTA.

The electronic transfer process has been studied using the heterogeneous rate constant (k^0) for the redox process: $[Fe(CN)_6]^{3-} + 1e^- \rightleftarrows [Fe(CN)_6]^{4-}$. The k^0 was calculated using CV, according to:

$$k^0 = \varphi\sqrt{\frac{D_0 \pi \nu n F}{RT}\left(\frac{D_{Red}}{D_{Ox}}\right)^{\alpha}} \quad (3)$$

where D_{Ox} and D_{Red} are the diffusion coefficient for the ferricyanide and ferrocyanide, respectively, ν is the scan rate (V/s), n is the number of electrons involved in the process, F is the Faraday constant (mol^{-1}), T is the temperature (K), R is the universal gas constant (J/Kmol) and α the dimensional transfer coefficient [30,31]. The latter was chosen to be equal to 0.5 [32], assuming the ratio of the anodic and cathodic peak equal approximately to 1 ($I_{pa}/I_{pc} = 1$), as successively calculated and reported (Table 1). The parameter φ can be obtained using the Nickolson method, where for each peak-to-peak separation (ΔE) there is correspondence with a φ value. For an accurate evaluation of this parameter, the equation based on the Nickolson theory [26,28-30] was used:

$$\varphi = \frac{(-0.6288 + 0.0021 \cdot \Delta E)}{(1 - 0.0170 \cdot \Delta E)} \quad (4)$$

Another method enabling k^0 values measurements for charge transfer reactions is EIS [33,34]. Experimental data were fitted using PSTrace software for a common Randles circuit (Fig. 2). This equivalent circuit, which is one of the simplest possible models describing processes at the electrochemical interface, consists of an active electrolyte resistance R_S in series with the parallel combination of the double-layer capacitance constant phase element (CPE). To the above-mentioned components, the charge transfer resistance (R_{ct}) and the Warburg impedance (W) are added. The latter are related to the electron transfer process and the diffusivity of the redox probe between the solution and the electrode surface, respectively.

In particular, assuming equimolar concentrations of oxidized and reduced species at the electrode surface (in our cases Fe^{2+}=Fe^{3+}) at a given time point, the determination of k^0 from EIS analysis is possible (Eq. 5), as reported by Randiviir 2018 [33,35,36].

$$R_{ct} = \frac{RT}{n^2 F^2 A C k^0} \quad (5)$$

This equation correlates the charge transfer resistance, R_{ct}, calculated from equivalent circuit fitting in EIS experiments to the exchange current density, i_0, according to:

$$i_0 = nFAk^0C \quad (6)$$

The Randles-Sevcik equation (Eq. 7) was used to determine the electrochemically effective surface area (A) and the diffusion coefficient, as previously reported [25,33]:

$$I_p = (0.4463)nFAC\sqrt{\frac{nF\nu D_0}{RT}} \quad (7)$$

where F is the constant of Faraday (mol^{-1}), R the universal constant of gas (J/Kmol), n the number of exchanged electrons, A the electrode surface (cm^2), C the analyte concentration (mol/cm^3), D_0 the diffusion coefficient (cm^2/s), and ν the scan rate (mV/s), respectively.

To investigate the electrochemical properties of the reversible redox probe employed in this work ($[Fe(CN)_6]^{3-/4-}$) the following equation have been used [37]:

$$E^0 = \frac{E_{pa} + E_{pc}}{2} \quad (8)$$

$$\Delta E = E_{pa} - E_{pc} \approx \frac{0.059}{n} \quad (9)$$

$$\frac{I_{pa}}{Ipc} = 1 \quad (10)$$

3. Results and discussion

3.1. Assembly of a label-free impedimetric SPGE-based immunosensor for OTA detection

CV and EIS were used as complementary tools to deeply characterize the electrochemical behaviour of the electrode/electrolyte interface at each step of the biosensor fabrication, comprehensively described in par. 2.4.1 and showed in Fig. 1. CV and EIS responses obtained by using [Fe $(CN)_6]^{3-/4-}$ as electroactive probe are shown in Fig. 3a and Fig. 3b, respectively. In particular, the frequency response from the EIS measurements were fitted to the Randles equivalent circuit (Fig. 2), from which the charge transfer resistance, R_{ct}, was extracted.

Furthermore, to robustly study the electron transfer process, the k^0 was assessed for each assembly step. Two notable theories allow us to completely measure and understand this parameter: Randles's theory and Marcus's theory, respectively. The first method, developed in 1947, describes how to determine the heterogeneous electron transfer constant impedimetrically [31,32]; the second-one, elaborated in 1956, reports the calculation of the k^0 using voltammetric techniques [33,36]. In this work, these theories are both used, and the data collected are reported in Table 1 and Table 2, respectively.

Voltammograms depicted in Fig. 3a, reveal the effects of the different chemical and biological layers over the electrical conductivity and resistivity of the electrode/electrolyte interface, influencing the SPGE performance. In particular, the construction of the immunological chain produces a significant decrease in the magnitude of both voltammetric peaks, reported as anodic and cathodic peak current (I_{pa} and I_{pc}), respectively. This is due to a dramatically decrease of the redox probe diffusivity close to WE interface, deriving by the sequential immobilization on the electrode surface of MBA, $EtNH_2$ and the final addition of the polyclonal Ab-OTA. Similarly, the Nyquist plots show an increase of the total impedance of the system (bare-OTA) indicating that an increased coverage of the electrode surface involves a slower electron transfer rate and higher charge transfer resistance compared to the bare platform. These phenomena are ascribable to the layer coating of the electrode surface, which became thicker with the assembly procedure, whereby reducing $[Fe(CN)_6]^{3-/4-}$ permeability through the immobilization of the layers.

Table 1
Anodic and cathodic peak ratio (I_{pa}/I_{pc}), peak-to-peak separation, effective surface area (A) and heterogeneous electron transfer rate constant (k^0) estimated for SPGE using CV in 0.005 M $[Fe(CN)_6]^{4-/3-}$, in PBS pH 7.0, during OTA-immunosensor fabrication. Average values of at least 6 SPGE are presented.

Layer	I_{pa}/I_{pc}	ΔE (mV)	A (cm^2)	k^0 (cm/s)
Bare	1.02 ± 0.01	89 ± 8	0.027 ± 0.01	$(1.2 \pm 0.3)\cdot10^{-2}$
H_2SO_4	1.04 ± 0.02	127 ± 9	0.022 ± 0.01	$(4.0 \pm 0.7)\cdot10^{-3}$
MBA	1.07 ± 0.02	189 ± 14	0.019 ± 0.001	$(1.9 \pm 0.4)\cdot10^{-3}$
EDC/NHS	0.99 ± 0.02	138 ± 8	0.021 ± 0.002	$(3.3 \pm 0.5)\cdot10^{-3}$
Ab-OTA	0.97 ± 0.06	284 ± 43	0.015 ± 0.002	$(1.9 \pm 0.5)\cdot10^{-4}$
$EtNH_2$	0.95 ± 0.07	258 ± 16	0.016 ± 0.002	$(3.3 \pm 1.5)\cdot10^{-4}$
OTA	0.95 ± 0.09	225 ± 29	0.018 ± 0.002	$(7.8 \pm 0.8)\cdot10^{-4}$

Table 2
Charge transfer resistance (R_{ct}), Warburg resistance (W) and heterogeneous electron transfer rate constant (k^0) estimated for SPGE using CV in 0.005 M [Fe $(CN)_6]^{4-/3-}$, in PBS pH 7.0, during OTA-immunosensor fabrication. Average values of at least 6 SPGEs are presented.

Layer	R_{ct} (KΩ)	W (Kσ)	k^0 (cm/s)
Bare	$(9.0 \pm 0.5)\cdot10^{-3}$	0.20 ± 0.06	$(1.20 \pm 0.07)\cdot10^{-2}$
H_2SO_4	$(1.12 \pm 0.24)\cdot10^{-1}$	0.27 ± 0.01	$(9.8 \pm 2.0)\cdot10^{-4}$
MBA	$(3.25 \pm 0.48)\cdot10^{-1}$	0.28 ± 0.01	$(3.3 \pm 0.5)\cdot10^{-4}$
EDC/NHS	$(1.19 \pm 0.18)\cdot10^{-1}$	0.29 ± 0.05	$(9.0 \pm 1.4)\ 10^{-4}$
Ab-OTA	$(13.4 \pm 0.89)\cdot10^{-1}$	0.30 ± 0.03	$(7.9 \pm 0.5)\ 10^{-5}$
$EtNH_2$	$(12.3 \pm 1.24)\cdot10^{-1}$	0.31 ± 0.03	$(8.7 \pm 0.9)\ 10^{-5}$
OTA (5 ng/mL)	$(6.40 \pm 0.59)\cdot10^{-1}$	0.29 ± 0.02	$(1.7 \pm 0.1)\ 10^{-4}$

3.2. Layer-by-layer electrochemical characterization of the OTA-immunosensor

Bare SPGE. For bare-SPGE, a typical electrochemically reversible couple voltammogram was obtained. In fact, both species (Fe^{2+} and Fe^{3+}) rapidly exchange electrons with the working electrode and the peak-to-peak separation is lower than 59 mV/e^- (Fig. 3a). In line, the Nyquist plot (Fig. 3b, black line) shows a smaller semicircle domain in comparison with the modified gold surfaces, indicating a small charge transfer resistance (R_{ct}), meaning a small resistance encountered by the electron as it travels between the redox species and electrode surface. Low R_{ct} values indicate a more electrochemically active surface[38].

Furthermore, the k^0 indicated roughly identical values when calculated using CV or EIS, thus confirming the accuracy of the methods.

H_2SO_4 treatment of SPGE. Electrodes were electrochemically treated by using the sulphuric acid potential cycling method as reported in section 2.5.1.

The potential-difference between the anodic and cathodic peak currents ($\Delta E_p = 127$ mV) and the charge transfer resistance ($R_{ct} = 0.112$ KΩ) calculated by using CV and EIS, showed an increase of ΔE and R_{ct} values compared to the bare platforms. This behaviour indicates the formation of gold oxide layer [39-41] which slows down the electronic transfer, as also shown by the decrease of k^0 reported in Table 1 and Table 2. These data are confirmed by the calculated electrodic area (A), which was reduced from 0.027 (bare) to 0.018 cm^2 (H_2SO_4-treated SPGE). These data lead also to hypothesize the occurrence of possible surface imperfections (roughness, indentations), due to the printed technology, as widely reported in different morphological characterizations of Dropsens 250 AT [42,43].

MBA deposition on SPGE. The possibility to functionalise gold working electrode with thiolated compounds through electrodeposition has attracted a considerable scientific interest, due to the capability to create more stable surfaces compared to SAM [22,44]. In this work, we exploited 4-MBA for developing OTA sensitive SPGE-based sensor with tuneable chemical functionalities, enabling the monitoring of the electrode-solution interface (electron transfer properties).

From the voltammograms reported in Fig. 3a, it is possible to observe a significant decrease in the magnitude of the voltammetric peaks (I_{pa}, I_{pc}) and an important increase of peak-to-peak separation (ΔE = 169 mV). This is ascribable to the highly shielding characteristic of the electrodeposited layer, which gradually hampers the electron transport onto the gold electrode surface [45,46]. This hypothesis is supported by the important decrease of k^0 and A (40-fold and 2-fold decrease, respectively) compared to the bare SPGEs, as reported in Table 1. To get more kinetic information on a wider time-constant range also EIS analysis was employed. A clear increase of total impedance was observed between bare SPGE ($R_{ct} = 0.009$ KΩ) and MBA functionalised electrode (MBA-SPGE, $R_{ct} = 0.325$ KΩ). This effect is due to the chemical properties of the MBA-SPGE preventing almost all-faradaic currents from penetrating to the surface (due to the thiol high insulating properties) [45]. In fact, the reaction rate of the ferro/ferricyanide couple for this step becomes gradually slower than the previous one, as shown by the increased peak-to-peak separation (quasi-reversible voltammograms shape) and the heterogeneous electron transfer constant calculated using CV and EIS (Table 1 and Table 2), according to previously reported data [25,46,47].

EDC/NHS activation of MBA-SPGE. After MBA electrodeposition, it was necessary to activate the carboxylic acid end-groups of MBA to enable the construction of the immunosensor. The chemistry of the carbodiimide provides one of the most popular and versatile method for the covalent attachment of proteins to SAMs. EDC is generally used in combination with NHS to immobilize proteins for biosensoristic purposes. This reaction favours the surface activation and subsequent covalent attachment of biological specimen on the self-assembled

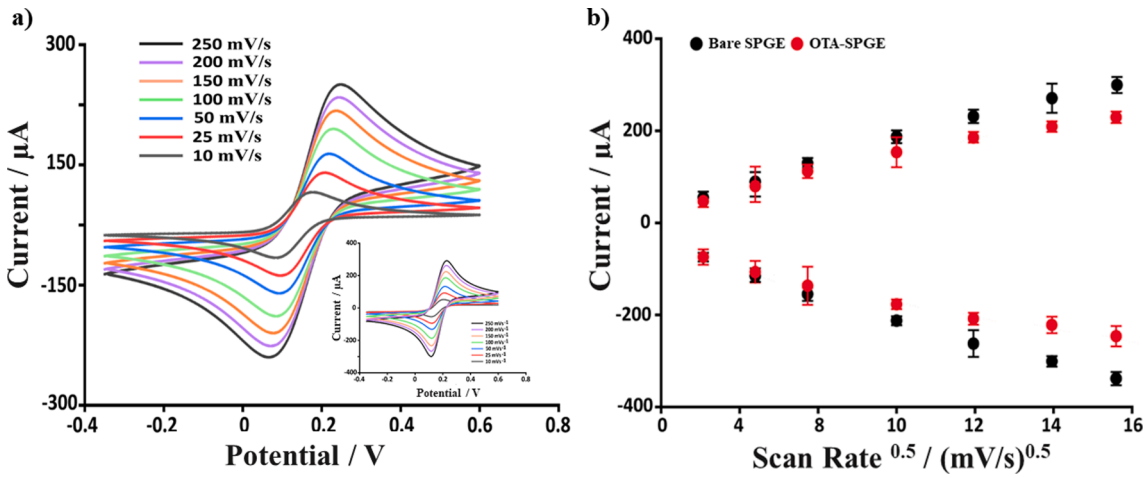

Fig. 4. Electrochemical processes occurring at the electrode surface. In a) the CV traces recorded at different scan rates (250, 200, 150, 100, 50, 25 e 10 mV/s) with bare (inset CVs) and with OTA immunosensor and in b) the linear dependence between I_{pa} and I_{pc} as a function of $\gamma^{0.5}$ for the same platforms, obtained using 0.005 M $[Fe(CN)_6]^{4-/3-}$ solution in 0.05 M PBS, pH 7.0. CVs of one representative SPGE fabricated sensor are presented along with current intensities of at least 3 analysed SPGEs. The error bars in panel b are the standard deviation calculated on three independent electrodes for each tested condition.

monolayers. The electrochemical surface characterization of EDC/NHS treated MBA-SPGE was performed by using CV and EIS. By analysing the voltammograms and the Nyquist's plot recorded for EDC/NHS step (green-line) reported in Fig. 3a, it is possible to observe that after the activation of MBA carboxyl groups by carbodiimide to form O-acylisourea intermediates, the electrostatic interaction between the positively charged intermediates and the negatively charged $[Fe(CN)_6]^{4-/3-}$ probes decreased the charge transfer resistance (MBA $R_{ct} = 0.325$ KΩ, and EDC/NHS $R_{ct} = 0.119$ KΩ), resulting in the occurrence of reduction and oxidation reactions of the probe more similar to the ideal reversible (quasi-reversible) voltammograms (MBA $\Delta E = 189$ mV, EDC/NHS $\Delta E = 138$ mV, MBA $I_{pa}/I_{pc} = 1.07$, and EDC/NHS $I_{pa}/I_{pc} = 0.99$ respectively) [48]. In fact, the negatively charged MBA layer hinders the access of the $[Fe(CN)_6]^{4-/3-}$ redox probe to the gold electrodes surface. Once the carbodiimide-mediated activation and acylation reactions occurred, the negatively charged barrier formed by MBA decreases facilitating again the electron transfer as demonstrated from the k^0 values calculated for the EDC/NHS step (3-fold higher compared to k^0 calculated for MBA) and reported in Table 1 and Table 2. The free electrode surface area (A) has roughly similar values for MBA-SPGE and EDC/NHS-MBA-SPGE as shown in Table 1; likewise, also the W values (Table 2) are comparable, indicating the carbodiimide-mediated activation does not affect the diffusional process.

Construction of the immuno-complex layer on MBA-SPGE. As for the other steps, CV and EIS were performed in the presence of $[Fe(CN)_6]^{4-/3-}$ as electroactive probe in order to ascertain the Ab-OTA immobilisation. The MBA layers and the consecutive immobilization of Ab-OTA caused a significant decrease of the electron transfer rate, measured by CV, with a 2-fold increase in peak-to-peak separation from $\Delta E = 138$ mV for EDC/NHS to $\Delta E = 284$ mV for Ab-OTA (see Table 1), and reduction of anodic and cathodic peaks due to hindering effects of the layer. The latter, along with MBA, creates a charge density barrier, which considerably slows down oxidation of Fe^{2+}, and the following reduction of Fe^{3+}, as shown by the k^0 value calculated using either CV or EIS (10-fold decreased compared to EDC/NHS step). A further confirmation is the sharp decrease in the free electrode area, which is 2-fold lower compared to the EDC/NHS SPGE (see Table 1). Furthermore, a 10-fold increase of total impedance was recorded compared to the previous step (EDC/NHS $R_{ct} = 0.138$ KΩ and Ab-OTA $R_{ct} = 0.134$ KΩ, respectively). This is because the hindrance of the Ab-OTA-MBA layer prevents redox probe from penetrating to the platform interface (SPGE), dramatically slowing down the discharge process (from quasi-reversible to non-reversible process).

After the immobilization of Ab-OTA, a cupping reaction with $EtNH_2$ was carried out to block unreacted active sites and reduce a-specific binding [49]. From CV and EIS spectra recorded for this step, no significant difference was observed when the $EtNH_2$ was dropped to Ab-OTA-MBA-SPGE, in contrast to the immobilization of Ab-OTA molecules, which gives rise to a substantial increase of total impedance. Voltammetric and impedimetric analyses provided roughly similar results for $EtNH_2$-blocking ($A = 0.016$ cm^2, $\Delta E = 258$ mV, $R_{ct} = 0.123$ KΩ, $k^0_{EIS} = 8.7{\cdot}10^{-5}$ cm/s; $k^0_{CV} = 3.3{\cdot}10^{-4}$ cm/s) and Ab-OTA immobilization steps ($A = 0.015$ cm^2, $\Delta E = 284$ mV, $R_{ct} = 0.134$ KΩ, $k^0_{EIS} = 7.9{\cdot}10^{-5}$ cm/s; $k^0_{CV} = 1.9{\cdot}10^{-4}$ cm/s).

Finally, we studied the electrochemical behaviour of the immuno-complex formation (OTA/Ab-OTA). In Fig. 3, the voltametric and impedimetric responses achieved after incubation with OTA solution at 5 ng/mL concentration, and the computed electrochemical parameters have been reported in Table 1 and 2. It is possible to observe that the immuno-complex formation did not give rise to changes in the active surface area, as expected (OTA/Ab-OTA, $A = 0.018$ cm^2, $\Delta E = 225$ mV). To the other hand, an important increase in electronic transfer rate was recorded as indicated by the k^0 value, which assumed value 4-fold of magnitude higher than antibody immobilization step ($k^0 = 1.9{\cdot}10^{-4}$, and $7.8{\cdot}10^{-4}$ cm/s for Ab-OTA and OTA step, respectively). EIS analyses further supported these data, in fact, the binding of OTA to its antibody induces a capacitance decrease, which is directly related to the amount of antigen used (see Fig. S3), according to previously reported data [25]. Specifically, a two-fold decrease of charge transfer resistance (R_{ct}) was recorded after OTA binding compared to the Ab-OTA deposition (0.640 KΩ and 0.134 KΩ for OTA and Ab-OTA, respectively). Thus, the immuno-complex formation causes differences in the dielectric and conductivity properties of the electrode surface resulting in a more effective electronic transfer process, as demonstrated by the k^0 value reported in Table 2.

3.3. Diffusivity process at the electrode interface

To study the nature of the electrochemical process occurring at the electrode surface, the effect of scan rate on the redox peak currents was studied. As shown in Fig. 4a faster the scan rates lower the size of the diffusion layer, consequently, increased current values are observed. Being the $[Fe(CN)_6]^{4-/3-}$ a reversible and freely diffusing redox species, the Randles-Sevcik equation (Eq. 7) describes how the anodic and cathodic peak currents (I_{pa}, I_{pc}) increase with the square root of the scan rate (γ). Plotting the I_{pa} and I_{pc} as a function of $\gamma^{0.5}$ (Fig. 4b) a linear

Table 3
Diffusion coefficient (D_0) estimated for SPGE using CV in 0.005 M $[Fe(CN)_6]^{4-/3-}$, in PBS pH 7.0, during OTA-immunosensor fabrication. Average values of at least 3 SPGEs are presented.

Layer	Anodic D_{Ox} (cm^2/s)	Cathodic D_{Red} (cm^2/s)	D_0 (cm^2/s)
Bare	$(5.17 \pm 0.02)\cdot10^{-6}$	$(5.01 \pm 0.01)\cdot10^{-6}$	$(5.09 \pm 0.01)\cdot10^{-6}$
MBA	$(3.59 \pm 0.01)\cdot10^{-6}$	$(3.35 \pm 0.01)\cdot10^{-6}$	$(3.47 \pm 0.01)\cdot10^{-6}$
Ab-OTA	$(2.46 \pm 0.02)\cdot10^{-6}$	$(2.60 \pm 0.01)\cdot10^{-6}$	$(2.53 \pm 0.01)\cdot10^{-6}$
OTA	$(2.57 \pm 0.01)\cdot10^{-6}$	$(2.10 \pm 0.01)\cdot10^{-6}$	$(2.34 \pm 0.01)\cdot10^{-6}$

dependence is observed with both bare SPGE and OTA-SPGE immunosensor. The deriving slopes ($\mu A/(mV/s)^{0.5}$) were calculated: 20.35 (R^2 = 0.999), −21.52 (R^2 = 0.999), 14.93 (R^2 = 0.997) and, −14.10 (R^2 = 0.996), corresponding respectively to I_{pa} and I_{pc} linear correlation obtained for bare SPGE and OTA immunosensor. This behavior indicates the oxidation/reduction reactions of the $[Fe(CN)_6]^{4-/3-}$ is mainly diffusion-controlled in agreement with planar diffusion controlled processes [50]. Thus, the rate of the electron transfer mechanism for the redox process is faster compared to the rate at which the electroactive species migrate from the bulk solution to the electrode interface due to concentration gradients [51].

By further manipulating [52] Eq. (7), the diffusion coefficient (D_0), was calculated and reported in Table 3. In particular, the anodic (D_{Ox}) and cathodic (D_{Red}) diffusion coefficients (D_0) of $[Fe(CN)_6]^{4-/3-}$, using 100 mV/s as scan rate, have been calculated. The results were compared to Konopka ($D_{Ox} = 7.26 \cdot 10^{-6}$ cm^2/s) and McDuffie ($D_{Red} = 6.67\cdot10^{-6}$ cm^2/s) coefficients [53]. Data reported in Table 3 highlight the bare electrode presents diffusional characteristics very similar to those of Konopka and McDuffie and, also, reveal an impairment of the diffusivity of the electrochemical probe proceeding with the construction of the biosensor, according to the calculating diffusion coefficients. In particular, the D_0 values decrease mainly after MBA and Ab-OTA deposition, reaching a 0.7 and 2-fold decrease compared to the bare SPGE, respectively. These CVs analyses revealed crucial to understand how the immunological chain construction influenced the diffusion of the redox probe at the electrode interface, a process that was less evident by performing EIS measurements. In fact, by comparing the Warburg resistance (W) reported in Table 2, negligible variations between each step have been observed. In addition, the Nyquist plot of bare and modified electrodes present a diffusive contribute (the straight line)

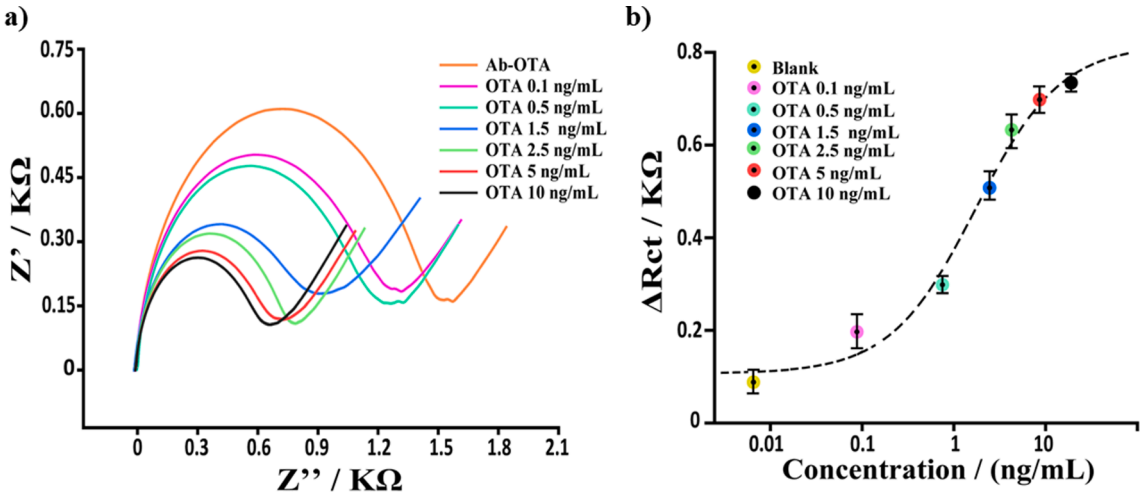

Fig. 5. Analytical performance of OTA immunosensor. a) Nyquist's Plot and b) calibration curve obtained using different OTA concentration in the range 0–10 ng/mL, in 0.005 M $[Fe(CN)_6]^{4-/3-}$ in 0.05 M PBS. Representative curves of at least 6 fabricated SPGEs are presented. The error bars in panel b are the standard deviation calculated on 6 independent electrodes for each tested OTA concentration.

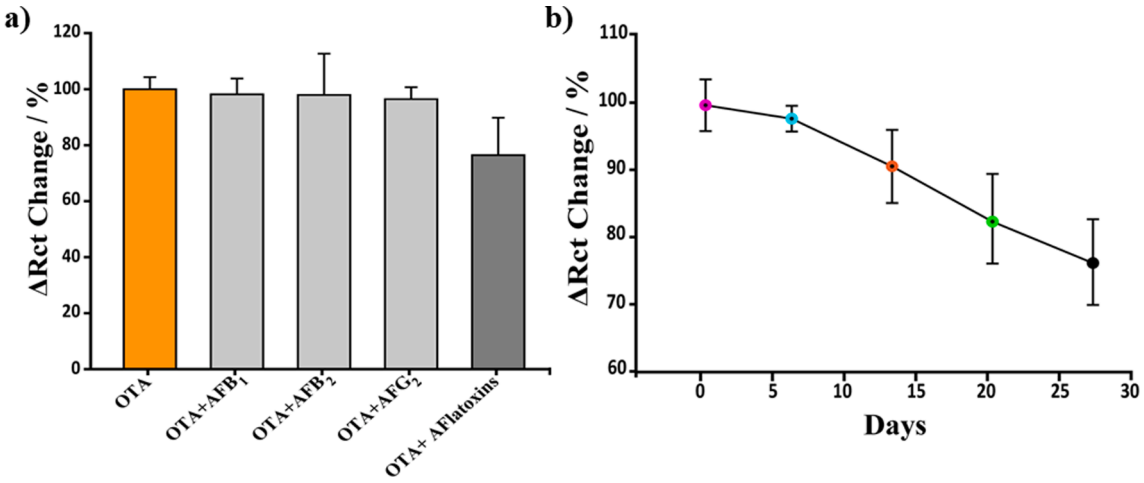

Fig. 6. Selectivity and stability of SPGE-based OTA immunosensor. a) Selectivity study. Effect of the presence of the aflatoxins AfB_1, AfB_2, AfG_2 and their mix on the impedimetric responses obtained for 2.5 μg/mL OTA solution. b) Stability study. The Ab-OTA-SPGE electrodes were tested after several days of storage at 4 °C in humid chamber and impedimetrically analysed at the indicated times with 2.5 μg/mL OTA concentration. The error bars are the standard deviation calculated on three independent electrodes for each tested condition.

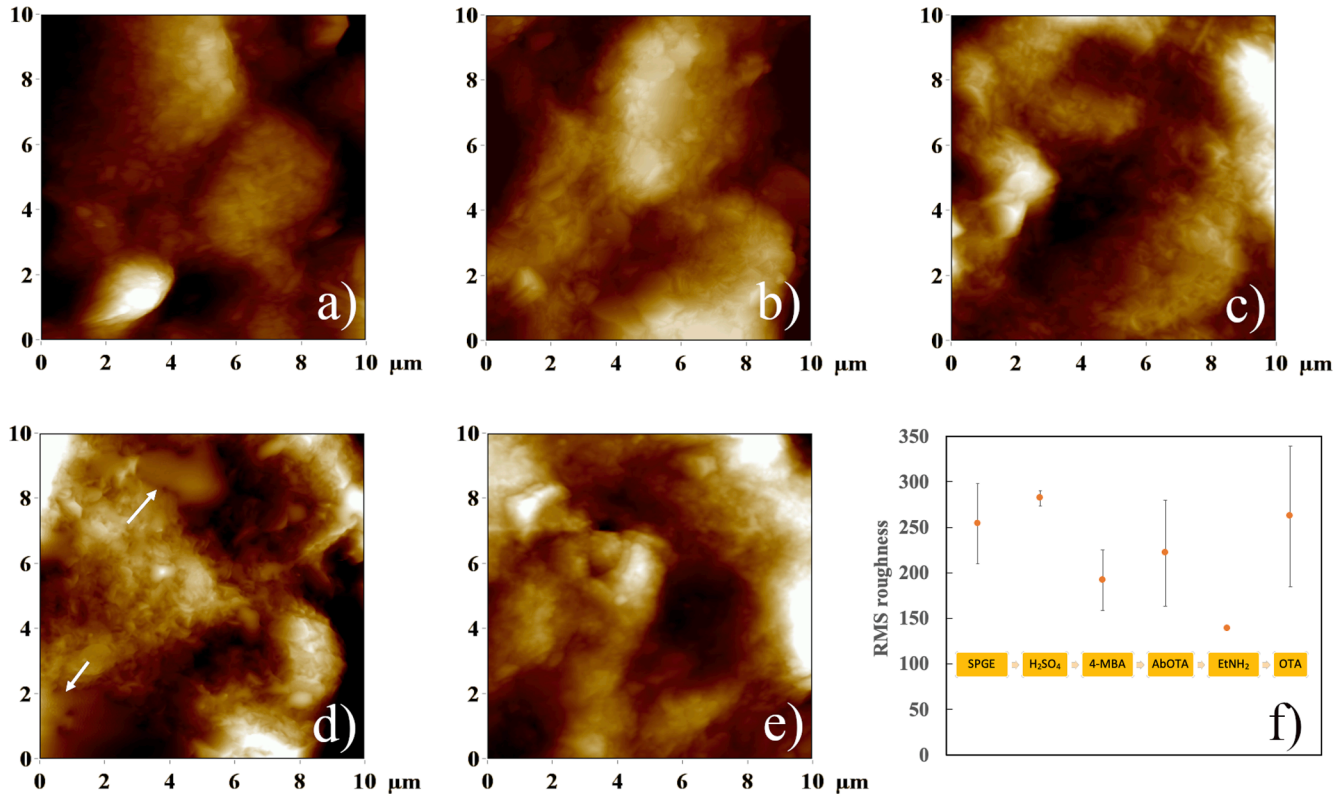

Fig. 7. AFM step-by-step surface characterization. 10 µm × 10 µm AFM images: a) bare SPGE, z scale = 741 nm b) SPGE after treatment in 0.05 M H_2SO_4, z scale = 740 nm; c) SPGE after MBA electrodeposition, z scale = 599 nm; d) MBA-SPGE after Ab-OTA immobilization, z scale = 333 nm e) OTA immunosensor surface, z scale = 562 nm; f) RMS roughness values of each step of the immunosensor assembly. The error bars are the standard deviations of the RMS roughness calculated by 4–6 images from randomly chosen regions of the same surface.

with a slope (angle), which are roughly the same for each layer deposition.

3.4. Analytical performance of SPGE-based OTA immunosensor

The analytical performance of the OTA immunosensor was tested with different OTA concentrations ranging from 0 to 10 ng/mL. The obtained results indicated the higher the OTA concentration the smaller the recorded R_{ct} (Fig. 5, Fig. S6). The reproducibility of the response of the immunosensor was investigated by analysis of the same concentration of OTA (2.5 ng/mL) using six equally prepared electrodes, and a relative standard deviation of 7% was calculated (Table S2). Moreover, the relative standard deviation calculated for each OTA concentration is also reported in Table S2.

The sensor exhibited similar analytical performance compared to previously reported electrochemical immunosensor [25,54-56]. In particular, the LOD and LOQ values were 0.19 and 0.40 ng/mL, respectively, the linear range was 0.37–2.86 ng/mL, and the sensitivity 1.01 kΩ mL/ng, leading to hypothesize a possible application of the developed immunosensor to real food samples, in agreement with the EU imposed MRL (Table S3).

3.5. Selectivity and stability of the SPGE-based OTA immunosensor

The selectivity of the fabricated sensors was evaluated by impedimetric measurements of a 2.5 ng/mL OTA solution in the presence of different compounds: Aflatoxin B_1, B_2, G_2 (AfB_1, AfB_2, AfG_2), and a mix of the three aflatoxins at a concentration ratio of 1:5 (analytes solution: interference tested). The signals obtained for these solutions were compared with those for the standard solution in the absence of any interferent. The results reported in Fig. 6a indicated high selectivity of the fabricated sensors, in fact the ΔR_{ct} values were not affected by the presence of single aflatoxins (approx. 97% of the ΔR_{ct} values registered for the 2.5 ng/mL OTA). However, the incubation with a mixed solution of aflatoxins determines a 30% reduction of this value.

To evaluate the stability of the biosensor in storage condition, the response of Ab-OTA-MBA-SPGE platforms was tested by storing the modified SPEs in PBS, pH = 7 at 4 °C in humid chamber up to 28 days and evaluating its ability to detect 2.5 ng/mL OTA solution. The data, reported in Fig. 6b, indicated a very good stability of the fabricated sensor during the first 14 days. Nevertheless, an important reduction of the performance was observed after 21 and 28 days, reporting decreases of the ΔR_{ct} values of 27% and 34%, respectively.

3.6. Atomic Force Microscopy (AFM) characterization of the immunosensor surface

AFM measurements have been performed in order to confirm step-by-step the successful coating of the SPGE. Representative morphology and topographic data of the immunosensor construction steps are shown in Fig. 7. Morphology of bare SPGE surface (Fig. 7a), electrode surface after H_2SO_4 treatment (Fig. 7b), MBA-SPGE (Fig. 7c), Ab-OTA-MBA-SPGE (Fig. 7d), $EtNH_2$ blocking layer (image not shown here) and OTA-Ab-OTA final sensor (Fig. 7e) were compared. In Fig. 7f) the RMS roughness values calculated for each fabrication step and averaged over 4–6 images from randomly chosen location of the same sample are reported. The error bars are the standard deviations of the averaged RMS roughness values.

The bare SPGE electrode is very rough (see Fig. 7a), with large difference, up to 1.4 µm, in surface height as already reported in literature for screen printed electrode [57]. RMS roughness averaged on six different regions of the same electrode is 254 nm with standard deviation of 44 nm, that provides a measure of the vertical unevenness of the electrode. The H_2SO_4 treatment of the SPGE surface reduces such

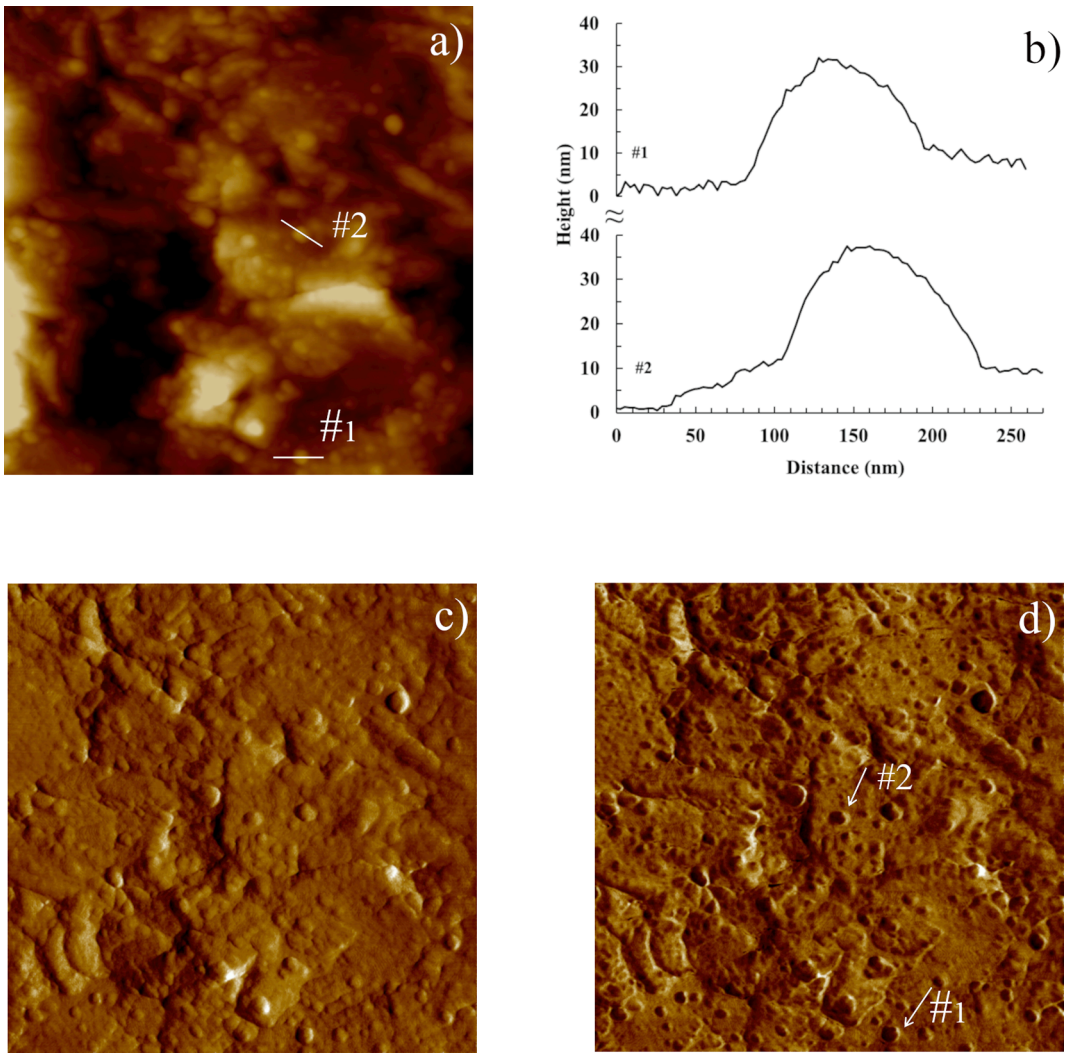

Fig. 8. High resolution 3 mm × 3 mm AFM scans of the immunosensor surface after OTA exposure. a) Topographic (height) image; b) plot profiles of the clusters labelled #1 and 2# along the lines shown in a); c) peak force error and d) phase contrast maps.

unevenness as shown by the decreases in the standard deviation of the RMS roughness (Fig. 7f), while preserving the morphological characteristic facets of the gold film (compare Fig. 7a and Fig. 7b). In the following fabrication step, successful MBA electrodeposition results in smoothing of the electrode surface as indicated by the decreases in the RMS roughness without affecting the surface morphology (Fig. 7c). The subsequent immobilization of Ab-OTA (Fig. 7d) is then proven by the increase in the average surface RMS roughness (Fig. 7f). However, the increase in the standard deviation of the RMS roughness, measured on six images, also points to an uneven distribution of Ab-OTA on the surface. Interestingly, after Ab-OTA immobilization, the AFM image of the electrode surface shows very flat region (indicated by arrow in Fig. 7d) probably ascribable to residual of salts from the deposition process that are not washed away by the gentle rinse with milli-Q water. The next deposition of the blocking $EtNH_2$ layer results in flattening of the surface (image not shown) and reduction in RMS roughness as shown in Fig. 7f, due to the selective deposition of the $EtNH_2$ molecules to block nonspecific sites. The subsequent exposure of the Ab-OTA-SPGE to OTA results in remarkable increase in the average RMS roughness calculated on five images and in its standard deviation. These data seem to point to successful specific OTA binding only to Ab-OTA covered regions.

To better investigate the surface of the electrode after Ab-OTA deposition (see Fig. S7) and OTA exposure, AFM images were recorded at higher resolution (1024x1024 points). AFM images (3x3 μm) of OTA-Ab-OTA surface are reported in Fig. 8. The surface topography (Fig. 8a) shows rounded particles (bright in the image), tens of nanometers height and hundred in diameter (Fig. 8b), attributable to clusters of Ab-OTA protruding from the rough electrode surface.

To overcome the drawback due to the high surface roughness and large height variation of SPGEs, Peak Force Error (PFE) and in-Phase Imaging mode AFM scans were also recorded simultaneously to the topography, as more suitable for finding small features on the rough surface sensors (see Fig. 8c and Fig. 8d). In addition, the changes in phase lag mapped in in-Phase Imaging mode can indicate changes in the mechanical properties of the scanned surface.

PFE image in Fig. 8c allows to clearly identify both isolated and partially coalesced particles. Some of these particles possess very different surface properties compared to the overall immunosensor surface as they appear as dark regions (regions with a low phase shift) in the in-Phase Imaging scan shown in Fig. 8d. Such dark regions, not observed in AFM Phase Imaging scan recorded on Ab-OTA-SPGE before exposure to OTA (see Fig. S7), could be ascribed to modification of the Ab-OTA viscoelastic properties due to OTA specific binding, hence supporting the conclusions of the electrochemical characterization of the immunosensor.

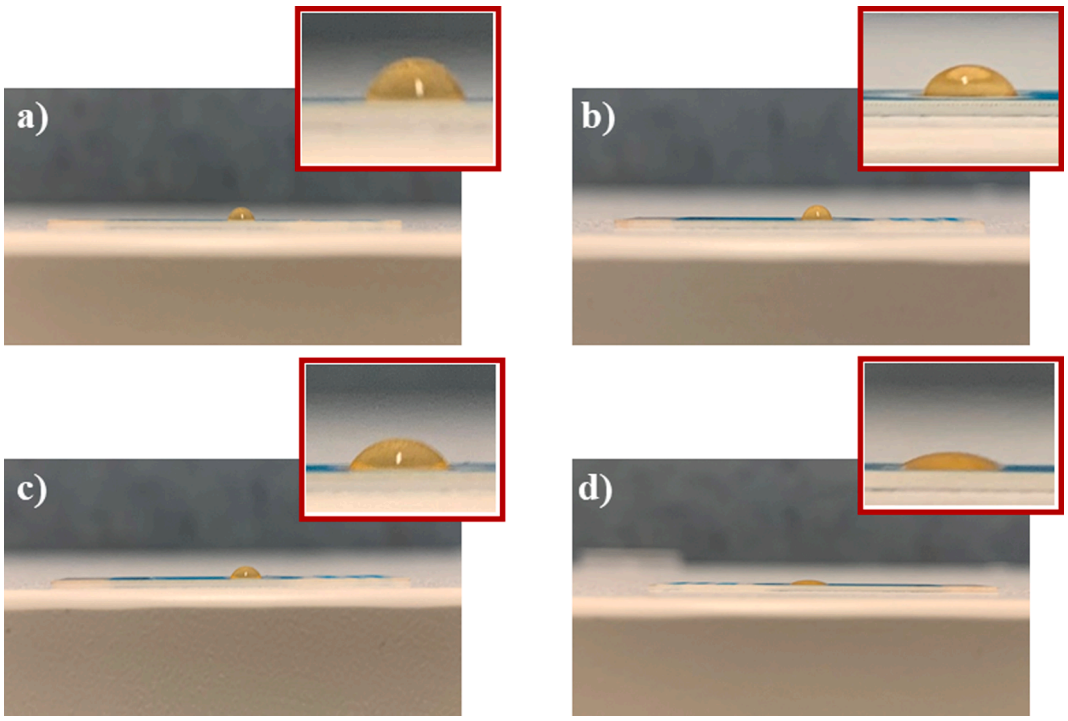

Fig. 9. Contact angle images for droplets water. a) bare SPGE; b) H_2SO_4 treated SPGE; c) MBA modified-SPGE; d) Ab-OTA immobilised platforms.

3.7. Static contact angle measurement

The hydrophilicity of the sensing platform during the preparation of OTA immunosensor was investigated by contact angle measurements. Fig. 9 shows the lower the angle, the higher the hydrophilicity. In most of the literature is reported that the contact angle of gold surface is mostly measured to be hydrophilic ($\theta < 90°$) and hardly hydrophobic ($\theta > 90°$) [58,59]. In our measurements (Table 4S), SPGE contact angle was $80.1° \pm 2.0°$, which is in agreement with values found in literature. The voltammetric cycling procedure in H_2SO_4 caused an improvement of the hydrophilicity of SPGEs ($69.6° \pm 5.1°$) suggesting the presence of gold oxide [39,60]. After the electrodeposition of MBA, the hydrophilicity increased ($59.6° \pm 5.6°$), due to the presence of carboxylic groups on the surface, which can provide a good biological microenvironment for biomolecules immobilization [61]. It also increased after the immobilization of Ab-OTA, showing the smallest contact angle value ($40.7° \pm 6.5°$), suggesting the successful fabrication of the immunosensor (Table S4).

4. Conclusions

In this work, disposable, simple, low-cost, label-free impedimetric immunosensor for OTA detection was successfully constructed and characterized morphologically and electrochemically. A quantitative characterization study of diffusion and electron transfer processes at the interface was undertaken by combining CV and EIS techniques, allowing us to understand and explain the chemistry underlying the interface modifications occurring during the biosensor construction. The sensor exhibited low detection limit, good sensitivity, reproducibility, selectivity and storage stability for commercial screen-printed platforms, paving the way to its potential exploitation for the detection of OTA in a wide range of foodstuffs. Finally, the sensor architecture, due to its simplicity and versatility, is suitable to be repurposed in different application fields.

CRediT authorship contribution statement

Rocco Cancelliere: Conceptualization, Methodology, Investigation, Formal analysis, Writing – original draft, Writing – review & editing, Visualization. **David Albano:** Methodology, Investigation, Formal analysis. **Benedetta Brugnoli:** Methodology, Investigation, Formal analysis, Writing – original draft. **Katia Buonasera:** Methodology, Investigation, Conceptualization, Formal analysis. **Gabriella Leo:** Investigation, Formal analysis, Writing – review & editing. **Andrea Margonelli:** Resources, Investigation. **Giuseppina Rea:** Conceptualization, Methodology, Validation, Resources, Writing – original draft, Writing – review & editing, Supervision, Funding acquisition.

Declaration of Competing Interest

The authors declare that they have no known competing financial interests or personal relationships that could have appeared to influence the work reported in this paper.

Acknowledgements

This work was supported by the Regione Lazio funded project FACILE grant n. 85-2017-15256. Acknowledgments are due to Mrs Luciana Cerri for her valuable technical support in performing AFM measurements, and Prof. Laura Micheli for critical reading of the manuscript and providing aflatoxins for the selectivity study.

Appendix A. Supplementary data

Supplementary data to this article can be found online at https://doi.org/10.1016/j.apsusc.2021.150791.

References

[1] D.M. Kolb, An atomistic view of electrochemistry, Surf. Sci. 500 (2002) 722–740, https://doi.org/10.1016/S0039-6028(01)01583-7.
[2] B. Kasemo, Biological surface science, Surf. Sci. 500 (2002) 656–677, https://doi.org/10.1016/S0039-6028(01)01809-X.

[3] A. Hayat, J. Marty, Disposable Screen Printed Electrochemical Sensors: Tools for Environmental Monitoring, Sensors. 14 (2014) 10432–10453, https://doi.org/10.3390/s140610432.

[4] E.T.S.G. da Silva, D.E.P. Souto, J.T.C. Barragan, J.de F. Giarola, A.C.M. de Moraes, L.T. Kubota, Electrochemical Biosensors in Point-of-Care Devices, Recent Advances and Future Trends, ChemElectroChem. 4 (2017) 778–794, https://doi.org/10.1002/celc.201600758.

[5] Y. Dai, C.C. Liu, Recent Advances on Electrochemical Biosensing Strategies toward Universal Point-of-Care Systems, Angew. Chem. Int. Ed. 58 (2019) 12355–12368, https://doi.org/10.1002/anie.201901879.

[6] A. Fernández-la-Villa, D.F. Pozo-Ayuso, M. Castaño-Álvarez, Microfluidics and electrochemistry: an emerging tandem for next-generation analytical microsystems, Curr. Opin. Electrochem. 15 (2019) 175–185, https://doi.org/10.1016/j.coelec.2019.05.014.

[7] G. Hanrahan, D.G. Patil, J. Wang, Electrochemical sensors for environmental monitoring: design, development and applications, J. Environ. Monitor. 6 (2004) 657, https://doi.org/10.1039/b403975k.

[8] L. Rotariu, F. Lagarde, N. Jaffrezic-Renault, C. Bala, Electrochemical biosensors for fast detection of food contaminants – trends and perspective, TrAC, Trends Anal. Chem. 79 (2016) 80–87, https://doi.org/10.1016/j.trac.2015.12.017.

[9] R. Hausbrand, W. Jaegermann, Reaction Layer Formation and Charge Transfer at Li-Ion Cathode—Electrolyte Interfaces: Concepts and Results Obtained by a Surface Science Approach, in, Encyclopedia of Interfacial Chemistry, Elsevier (2018) 232–245, https://doi.org/10.1016/B978-0-12-409547-2.14195-2.

[10] L.M. Da Silva, L.A. De Faria, J.F.C. Boodts, Electrochemical impedance spectroscopic (EIS) investigation of the deactivation mechanism, surface and electrocatalytic properties of Ti/RuO2(x)+Co3O4(1–x) electrodes, Journal of Electroanalytical Chemistry. 532 (2002) 141–150, https://doi.org/10.1016/S0022-0728(02)00810-0.

[11] S.B. Tang, M.O. Lai, L. Lu, Study on Li+-ion diffusion in nano-crystalline LiMn2O4 thin film cathode grown by pulsed laser deposition using CV, EIS and PITT techniques, Materials Chemistry and Physics. 111 (2008) 149–153, https://doi.org/10.1016/j.matchemphys.2008.03.041.

[12] Z. Mikušová, Z. Farka, M. Pastucha, V. Poláchová, R. Obořilová, P. Skládal, Amperometric Immunosensor for Rapid Detection of Honeybee Pathogen *Melissococcus Plutonius*, Electroanalysis 31 (2019) 1969–1976, https://doi.org/10.1002/elan.201900252.

[13] Q. Li, T. Zhang, Y. Pan, L.C. Ciacchi, B. Xu, G. Wei, AFM-based force spectroscopy for bioimaging and biosensing, RSC Adv. 6 (2016) 12893–12912, https://doi.org/10.1039/C5RA22841G.

[14] T. Huhtamäki, X. Tian, J.T. Korhonen, R.H.A. Ras, Surface-wetting characterization using contact-angle measurements, Nat Protoc. 13 (2018) 1521–1538, https://doi.org/10.1038/s41596-018-0003-z.

[15] F. Ricci, G. Volpe, L. Micheli, G. Palleschi, A review on novel developments and applications of immunosensors in food analysis, Anal. Chim. Acta 605 (2007) 111–129, https://doi.org/10.1016/j.aca.2007.10.046.

[16] G. Mishra, A. Barfidokht, F. Tehrani, R. Mishra, Food Safety Analysis Using Electrochemical Biosensors, Foods. 7 (2018) 141, https://doi.org/10.3390/foods7090141.

[17] S.S. Moises, M. Schäferling, Toxin immunosensors and sensor arrays for food quality control, Bioanalytical Reviews. 1 (2009) 73–104, https://doi.org/10.1007/s12566-009-0006-x.

[18] L. Zhihong, H. Kunlun, L. Yunbo, Ochratoxin A and ochratoxin-producing fungi on cereal grain in China: a review, Food Additives & Contaminants: Part A. 32 (2015) 461–470, https://doi.org/10.1080/19440049.2014.996787.

[19] Opinion of the Scientific Panel on contaminants in the food chain [CONTAM] related to ochratoxin A in food, EFSA Journal. (n.d.). https://doi.org/10.2903/j.efsa.2006.365.

[20] A. Vecchio, V. Mineo, D. Planeta, Ochratoxin A in instant coffee in Italy, Food Control 28 (2012) 220–223, https://doi.org/10.1016/j.foodcont.2012.04.029.

[21] M. Kujawa, Some Naturally Occurring Substances: Food Items and Constituents, Heterocyclic Aromatic Amines and Mycotoxins. IARC Monographs on the Evaluation of Carcinogenic Risks to Humans, Vol. 56. Herausgegeben von der International Agency for Research on Cancer, World Health Organization. 599 Seiten, zahlr. Abb. und Tab. World Health Organization. Geneva 1993. Preis: 95, — Sw.fr; 95,50 US $, Nahrung. 38 (1994) 351–351. https://doi.org/10.1002/food.19940380335.

[22] Y. Alhamoud, D. Yang, S.S. Fiati Kenston, G. Liu, L. Liu, H. Zhou, F. Ahmed, J. Zhao, Advances in biosensors for the detection of ochratoxin A: Bio-receptors, nanomaterials, and their applications, Biosens. Bioelectron. 141 (2019), 111418, https://doi.org/10.1016/j.bios.2019.111418.

[23] R. Biffi, M. Munari, L. Dioguardi, C. Ballabio, A. Cattaneo, C.L. Galli, P. Restani, Ochratoxin A in conventional and organic cereal derivatives: a survey of the Italian market, 2001–02, Food Addit. Contam. 21 (2004) 586–591, https://doi.org/10.1080/02652030410001687708.

[24] D. Mandler, S. Kraus-Ophir, Self-assembled monolayers (SAMs) for electrochemical sensing, J Solid State Electrochem. 15 (2011) 1535–1558, https://doi.org/10.1007/s10008-011-1493-6.

[25] F. Malvano, D. Albanese, R. Pilloton, M. Di Matteo, A highly sensitive impedimetric label free immunosensor for Ochratoxin measurement in cocoa beans, Food Chem. 212 (2016) 688–694, https://doi.org/10.1016/j.foodchem.2016.06.034.

[26] F. Malvano, D. Albanese, R. Pilloton, Impedimetric label - free immunosensor for rapid detection of Ochratoxin A in beer and wine, in: 2020 IEEE International Workshop on Metrology for Agriculture and Forestry (MetroAgriFor), IEEE, Trento, Italy, 2020: pp. 323–327. https://doi.org/10.1109/MetroAgriFor50201.2020.9277594.

[27] P.R. Solanki, A. Kaushik, T. Manaka, M.K. Pandey, M. Iwamoto, V.V. Agrawal, B. D. Malhotra, Self-assembled monolayer based impedimetric platform for food borne mycotoxin detection, Nanoscale. 2 (2010) 2811, https://doi.org/10.1039/c0nr00289e.

[28] ImagesSXM, (n.d.). https://www.liverpool.ac.uk/~sdb/ImageSXM/ (accessed May 14, 2021).

[29] B. Law (Ed.), Immunoassay: a practical guide, Taylor & Francis, London, 1996.

[30] R. Cancelliere, A. Di Tinno, A.M. Di Lellis, Y. Tedeschi, S. Bellucci, K. Carbone, E. Signori, G. Contini, L. Micheli, An inverse-designed electrochemical platform for analytical applications, Electrochem. Commun. 121 (2020), 106862, https://doi.org/10.1016/j.elecom.2020.106862.

[31] R.S. Nicholson, Theory and Application of Cyclic Voltammetry for Measurement of Electrode Reaction Kinetics, Anal. Chem. 37 (1965) 1351–1355, https://doi.org/10.1021/ac60230a016.

[32] R. Cancelliere, K. Carbone, M. Pagano, I. Cacciotti, L. Micheli, Biochar from Brewers' Spent Grain: A Green and Low-Cost Smart Material to Modify Screen-Printed Electrodes, Biosensors. 9 (2019) 139, https://doi.org/10.3390/bios9040139.

[33] E.P. Randviir, A cross examination of electron transfer rate constants for carbon screen-printed electrodes using Electrochemical Impedance Spectroscopy and cyclic voltammetry, Electrochim. Acta 286 (2018) 179–186, https://doi.org/10.1016/j.electacta.2018.08.021.

[34] R.S. Nicholson, Irving. Shain, Theory of Stationary Electrode Polarography. Single Scan and Cyclic Methods Applied to Reversible, Irreversible, and Kinetic Systems, Anal. Chem. 36 (1964) 706–723, https://doi.org/10.1021/ac60210a007.

[35] R.A. Marcus, On the Theory of Oxidation-Reduction Reactions Involving Electron Transfer, I, The Journal of Chemical Physics. 24 (1956) 966–978, https://doi.org/10.1063/1.1742723.

[36] R.A. Marcus, On the Theory of Oxidation-Reduction Reactions Involving Electron Transfer. II. Applications to Data on the Rates of Isotopic Exchange Reactions, J. Chem. Phys. 26 (1957) 867–871, https://doi.org/10.1063/1.1743423.

[37] J. Wang, Analytical Electrochemistry: Wang/Analytical Electrochemistry, Third Edition, John Wiley & Sons Inc, Hoboken, NJ, USA, 2006 https://doi.org/10.1002/0471790303.

[38] E. Barsoukov, J.R. Macdonald (Eds.), Impedance Spectroscopy: Theory, Experiment, and Applications, John Wiley & Sons Inc, Hoboken, NJ, USA, 2018, https://doi.org/10.1002/9781119381860.

[39] W. Zhang, A.D. Bas, E. Ghali, Y. Choi, Passive behavior of gold in sulfuric acid medium, Transactions of Nonferrous Metals Society of China. 25 (2015) 2037–2046, https://doi.org/10.1016/S1003-6326(15)63813-4.

[40] Y. Wang, Y. Sun, H. Liao, S. Sun, S. Li, J.W. Ager, Z.J. Xu, Activation Effect of Electrochemical Cycling on Gold Nanoparticles towards the Hydrogen Evolution Reaction in Sulfuric Acid, Electrochim. Acta 209 (2016) 440–447, https://doi.org/10.1016/j.electacta.2016.05.095.

[41] Y. Wang, E. Laborda, A. Crossley, R.G. Compton, Surface oxidation of gold nanoparticles supported on a glassy carbon electrode in sulphuric acid medium: contrasts with the behaviour of 'macro' gold, Phys. Chem. Chem. Phys. 15 (2013) 3133, https://doi.org/10.1039/c3cp44615h.

[42] L.M. Fischer, M. Tenje, A.R. Heiskanen, N. Masuda, J. Castillo, A. Bentien, J. Émneus, M.H. Jakobsen, A. Boisen, Gold cleaning methods for electrochemical detection applications, Microelectron. Eng. 86 (2009) 1282–1285, https://doi.org/10.1016/j.mee.2008.11.045.

[43] P. Fanjul-Bolado, D. Hernández-Santos, P.J. Lamas-Ardisana, A. Martín-Pernía, A. Costa-García, Electrochemical characterization of screen-printed and conventional carbon paste electrodes, Electrochim. Acta 53 (2008) 3635–3642, https://doi.org/10.1016/j.electacta.2007.12.044.

[44] N. Metoki, L. Liu, E. Beilis, N. Eliaz, D. Mandler, Preparation and Characterization of Alkylphosphonic Acid Self-Assembled Monolayers on Titanium Alloy by Chemisorption and Electrochemical Deposition, Langmuir 30 (2014) 6791–6799, https://doi.org/10.1021/la404829b.

[45] E. Boubour, R.B. Lennox, Insulating Properties of Self-Assembled Monolayers Monitored by Impedance Spectroscopy, Langmuir 16 (2000) 4222–4228, https://doi.org/10.1021/la991328c.

[46] F. Malvano, D. Albanese, R. Pilloton, M. Di Matteo, A. Crescitelli, A New Label-Free Impedimetric Affinity Sensor Based on Cholinesterases for Detection of Organophosphorous and Carbamic Pesticides in Food Samples: Impedimetric Versus Amperometric Detection, Food Bioprocess Technol. 10 (2017) 1834–1843, https://doi.org/10.1007/s11947-017-1955-7.

[47] H. Abdulkarim, M. Zourob, M. Siaj, Development of Label-Free Impedimetric Immunosensors for IKZF1 and IKZF3 Femtomolar Detection for Monitoring Multiple Myeloma Patients Treated with Lenalidomide, Sci. Rep. 10 (2020) 10424, https://doi.org/10.1038/s41598-020-67241-w.

[48] L. Liu, D. Deng, Y. Xing, S. Li, B. Yuan, J. Chen, N. Xia, Activity analysis of the carbodiimide-mediated amine coupling reaction on self-assembled monolayers by cyclic voltammetry, Electrochim. Acta 89 (2013) 616–622, https://doi.org/10.1016/j.electacta.2012.11.049.

[49] E. Sánchez-Tirado, A. González-Cortés, P. Yánez-Sedeño, J.M. Pingarrón, Electrochemical Immunosensor for Sensitive Determination of TGF β1 in Urine, Procedia Technol. 27 (2017) 81–84, https://doi.org/10.1016/j.protcy.2017.04.035.

[50] C.G. Zoski (Ed.), Handbook of electrochemistry, 1. ed, Elsevier, Amsterdam, 2007.

[51] I. Husu, G. Rodio, E. Touloupakis, M.D. Lambreva, K. Buonasera, S.C. Litescu, M. T. Giardi, G. Rea, Insights into photo-electrochemical sensing of herbicides driven by Chlamydomonas reinhardtii cells, Sens. Actuators, B 185 (2013) 321–330, https://doi.org/10.1016/j.snb.2013.05.013.

[52] R. Cancelliere, F. Zurlo, L. Micheli, S. Melino, Vegetable waste scaffolds for 3D-stem cell proliferating systems and low cost biosensors, Talanta 223 (2021), 121671, https://doi.org/10.1016/j.talanta.2020.121671.
[53] S.J. Konopka, Bruce. McDuffie, Diffusion coefficients of ferri- and ferrocyanide ions in aqueous media, using twin-electrode thin-layer electrochemistry, Anal. Chem. 42 (1970) 1741–1746, https://doi.org/10.1021/ac50160a042.
[54] F. Malvano, D. Albanese, A. Crescitelli, R. Pilloton, E. Esposito, Impedimetric Label-Free Immunosensor on Disposable Modified Screen-Printed Electrodes for Ochratoxin A, Biosensors. 6 (2016) 33, https://doi.org/10.3390/bios6030033.
[55] S. Alarcon, G. Palleschi, D. Compagnone, M. Pascale, A. Visconti, I. Barnavetro, Monoclonal antibody based electrochemical immunosensor for the determination of ochratoxin A in wheat, Talanta 69 (2006) 1031–1037, https://doi.org/10.1016/j.talanta.2005.12.024.
[56] J.C. Vidal, L. Bonel, A. Ezquerra, P. Duato, J.R. Castillo, An electrochemical immunosensor for ochratoxin A determination in wines based on a monoclonal antibody and paramagnetic microbeads, Anal Bioanal Chem. 403 (2012) 1585–1593, https://doi.org/10.1007/s00216-012-5951-5.
[57] Z. Farka, T. Juřík, M. Pastucha, D. Kovář, K. Lacina, P. Skládal, Rapid Immunosensing of *Salmonella* Typhimurium Using Electrochemical Impedance Spectroscopy: the Effect of Sample Treatment, Electroanalysis 28 (2016) 1803–1809, https://doi.org/10.1002/elan.201600093.
[58] M.G. Paulik, P.A. Brooksby, A.D. Abell, A.J. Downard, Grafting Aryl Diazonium Cations to Polycrystalline Gold: Insights into Film Structure Using Gold Oxide Reduction, Redox Probe Electrochemistry, and Contact Angle Behavior, J. Phys. Chem. C. 111 (2007) 7808–7815, https://doi.org/10.1021/jp0706578.
[59] J. Canning, N. Tzoumis, J.K. Beattie, B.C. Gibson, E. Ilagan, Water on Au sputtered films, Chem. Commun. 50 (2014) 9172–9175, https://doi.org/10.1039/C4CC02492C.
[60] R.F. Tabor, A.J. Morfa, F. Grieser, D.Y.C. Chan, R.R. Dagastine, Effect of Gold Oxide in Measurements of Colloidal Force, Langmuir 27 (2011) 6026–6030, https://doi.org/10.1021/la200166r.
[61] H. Shen, C. Wang, C. Ren, G. Zhang, Y. Zhang, J. Li, X. Hu, Z. Yang, A streptavidin-functionalized tin disulfide nanoflake-based ultrasensitive electrochemical immunosensor for the detection of tumor markers, New J. Chem. 44 (2020) 6010–6014, https://doi.org/10.1039/D0NJ00160K.